Materials Today Physics 15 (2020) 100265

Contents lists available at ScienceDirect

Materials Today Physics

journal homepage: https://www.journals.elsevier.com/materials-today-physics

Stretchable, ultrasensitive, and low-temperature NO_2 sensors based on MoS_2@rGO nanocomposites

Ning Yi [a, 1], Zheng Cheng [b, 1], Han Li [c, d, e, 1], Li Yang [c, f], Jia Zhu [c], Xiaoqi Zheng [c, g], Yong Chen [b], Zhendong Liu [c, h], Hongli Zhu [b, **], Huanyu Cheng [a, c, *]

[a] *Department of Materials Science and Engineering, And Materials Research Institute, The Pennsylvania State University, University Park, PA, 16802, USA*
[b] *Department of Mechanical and Industrial Engineering, Northeastern University, Boston, MA, 02115, USA*
[c] *Department of Engineering Science and Mechanics, The Pennsylvania State University, University Park, PA, 16802, USA*
[d] *Pen-Tung Sah Institute of Micro-Nano Science and Technology, Xiamen University, Xiamen, Fujian, 361005, China*
[e] *Southeast Institute of Chinaunicom, Fuzhou, Fujian, 350000, China*
[f] *Hebei Key Laboratory of Robot Perception and Human-robot Interaction, School of Mechanical Engineering, Hebei University of Technology, Tianjin, 300401, China*
[g] *School of Physical Science and Technology, ShanghaiTech University, Shanghai, 201219, China*
[h] *Zhejiang University of Technology, Ministry of Education and Zhejiang Province, Hangzhou, Zhejiang, 310014, China*

ARTICLE INFO

Article history:
Received 28 April 2020
Received in revised form
31 July 2020
Accepted 14 August 2020
Available online 19 August 2020

Keywords:
Molybdenum disulfide (MoS_2)
Reduced graphene oxide (rGO)
Nitrogen dioxide (NO_2)
Stretchable and ultrasensitive
Laser-induced graphene (LIG) patterns

ABSTRACT

The recent development of 3D highly porous laser-induced graphene (LIG) has drawn significant attention for numerous sensing applications. In particular, novel gas sensing platforms based on stretchable LIG patterns with self-heating capabilities have been demonstrated as a simple alternative to interdigitated electrodes (IDEs) for integrating gas-sensitive nanomaterials. However, their direct performance comparison with the IDEs is unclear. In this paper, the sensing performance of nanomaterials with various specific surface areas between the LIG patterns and IDEs are compared directly. Molybdenum disulfide (MoS_2) @ reduced graphene oxide (rGO) was synthesized with controllable size and morphology for nitrogen dioxide (NO_2) sensing. When dispersing MoS_2@rGO on an IDE integrated on a soft silicone polymeric substrate, the stretchable gas sensor exhibited mechanical robustness upon stretching and a significantly large signal-to-noise ratio (SNR) for rapid detection of 10 ppb NO_2. The MoS_2@rGO nanocomposite was integrated on a stretchable 3D porous LIG pattern yielding an extraordinarily high SNR of 1026.9 to NO_2 of 2 ppm. Considering the high SNR of over 60 to NO_2 of 10 ppb, the novel LIG gas sensing platform with a simple fabrication process shows a great promise to test nanomaterials and enable stretchable bio-integrated gas sensors for monitoring of the health and environment.

1. Introduction

Deformable gas sensors that can deploy on the skin or soft surfaces to detect various gaseous compounds are integral to accurate and real-time monitoring of health or environmental conditions. For instance, nitrogen dioxide (NO_2), a common toxic gas formed by oxidation of emitted NO and N_2O from the internal combustion motor engines, frequently results in adverse respiratory health issues such as chronic bronchitis, emphysema, and irritation [1–3]. It is reported that 10–20 parts per million (ppm) NO_2 is mildly irritating [4], and exposure to 150 ppm or higher may cause death from pulmonary edema or bronchospasm [5]. Studies also reveal a significant association between long-term NO_2 exposure and mortality due to heart failure and dysrhythmia [6,7]. Therefore, it is necessary to develop wearable NO_2 gas sensors to continuously detect the NO_2 level around individuals, especially those living in urban areas with elevated NO_2 concentration. With the prevalence of the Internet of Things (IoT) in the future, the data collected from wearable NO_2 gas sensors can also guide the government or environmental department to better control air pollution. The requirements for wearable NO_2 sensors include high accuracy, fast response and recovery, good selectivity, low power consumption, small size, low cost, and mechanical robustness [8].

---

[*] Corresponding author.
[**] Corresponding author.
E-mail addresses: h.zhu@neu.edu (H. Zhu), huanyu.cheng@psu.edu (H. Cheng).
[1] These authors contributed equally to this work.

https://doi.org/10.1016/j.mtphys.2020.100265
2542-5293/

Though widely commercialized electrochemical gas sensors exhibit fast response and recovery rates, low cost, and small power consumption [9]. They are not easy to miniaturize for wearable epidermal gas sensors and suffer from poor performance at an ultralow concentration relevant to health concerns [10]. As the most suitable modality for wearable devices, chemiresistive gas sensors have been explored for NO_2 sensing due to their simple fabrication process compared with electrochemical cells, field-effect transistors, and the other types of gas sensors [11]. Metal oxide-based chemiresistive gas sensors have been extensively studied for gas detection, but they suffer from large power consumption, poor selectivity, and high noise [12–14]. As an alternative, transition-metal dichalcogenides (TMD) with nanostructures as a new class of functional materials start to gain momentum in the development of high-performance gas sensors due to their large specific surface area, substantial surface activities, improved signal-to-noise ratio (SNR), and tunable electrical conductivity [15,16].

Among the TMD materials, molybdenum disulfide (MoS_2) demonstrates excellent potential for NO_2 identification at room temperature [17]. However, significant adsorption of ambient oxygen strongly influences the properties of pristine MoS_2, leading to dramatic degradation in its conductivity upon accumulative exposure to air [18,19]. To overcome the limitation of MoS_2-based gas sensors for practical application, various materials (SnO_2 [20], Co_3O_4 [21], ZnO [22], graphene [23], etc.) have been coupled with MoS_2 nanocrystals to improve their stability from decreased surface electron density and to enhance the gas sensing response from formed heterostructures. As widely reported in the literature, graphene prepared from multiple approaches that include mechanical exfoliation [24], chemical vapor deposition [25], and epitaxial growth [26] has shown a low limit of detection, small noise, and good reversibility. Due to the existence of reactive sites provided by the hydroxyl groups, reduced graphene oxide (rGO) usually has enhanced selectivity and sensitivity compared with pristine graphene [27]. By combining the high specific surface area of graphene scaffold and the excellent sensitivity and selectivity from MoS_2 to NO_2, a graphene/MoS_2 hybrid aerogel consisting of MoS_2 and GO has been realized to detect the ultralow concentration of NO_2 down to 50 ppb [28]. However, these composites need to operate at a relatively high temperature of 200 °C to reach reasonable response and recovery rates. A slow recovery is one of the critical problems in the MoS_2-based NO_2 gas sensors at room temperature, and additional treatment such as UV light is always necessary to shorten the response and recovery time [29]. Because fast response and recovery rates are desirable for many gas sensing applications such as toxic or explosive gas, it is of great interest to identify sensing materials with fast response/recovery rates at room temperature. Although efforts have been attempted (e.g., facilitated NO_2 reversible sensing behavior with oxygen functional groups in GO [30] or vertically aligned MoS_2 because of the high aspect ratio and adsorption energy on exposed edge sites [31]), the development of high-performance room temperature NO_2 gas sensor based on graphene/MoS_2 composites still remains elusive.

By leveraging the recent development of 3D highly porous laser-induced graphene (LIG), a novel gas sensing platform that is based on stretchable LIG patterns has been demonstrated as a simple alternative to interdigitated electrodes (IDEs) for integrating gas-sensitive nanomaterials [32]. Although the novel LIG gas sensing platform is shown to be effective in integrating and test both metal oxides and low-dimensional nanomaterials, its direct performance comparison with the IDEs is not clear. Here we will directly compare the sensing performance of low-dimensional nanomaterials with various specific surface areas between the LIG patterns and IDEs. We first report the synthesis of nanostructured MoS_2@rGO composites with various controlled specific surface areas and their applications for reversible, ultrasensitive, stretchable, room temperature NO_2 gas sensors. By adjusting the ball-milled NaCl crystal fillers in a solvothermal process, the controlled synthesis resulted in the MoS_2@rGO composites with a tunable surface area in a wide range. Integrating the composite sensing material on an IDE first confirmed the room temperature sensing capability of the MoS_2@rGO composites to NO_2. The effect of the specific surface area of the porous MoS_2@rGO composites on their gas sensing performance was then investigated. The sample with the largest specific surface area demonstrated a significantly improved signal-to-noise ratio (SNR). The SNR was also enhanced from 60 to over 300 (to 2 ppm NO_2) as the spacing between the fingers in the IDE reduced from 200 to 80 μm. The significantly enhanced SNR allowed the gas sensor to detect an ultralow concentration of 10 parts per billion (ppb) NO_2 with an SNR of 35.4 at room temperature. While it is possible to further reduce the spacing between the fingers, the process complexity to fabricate the IDE with reduced spacing would increase substantially. Being configured in a stretchable layout, the fabricated MoS_2@rGO gas sensor demonstrated robust mechanical operation upon stretching of 20%. The outstanding performance of MoS_2@rGO gas sensors with controlled specific surface areas compares favorably against the previously published literature reports (Table 1). As an alternative, the MoS_2@rGO nanomaterial can be directly integrated on a 3D porous LIG line to eliminate the use of IDEs. The stretchable LIG-based MoS_2@rGO NO_2 gas sensor exhibited an extraordinarily high SNR of 1026.9 to NO_2 of 2 ppm with minimal interference from water vapor upon self-heating at a low temperature of 40 °C. Considering the high SNR of 62 to NO_2 of 10 ppb [32], the new LIG gas sensing platform with a simple fabrication process is indeed very effective in testing nanomaterials and enable stretchable bio-integrated gas sensors.

2. Material and methods

2.1. Synthesis of GO and rGO

The GO was prepared according to the modified Hummers' method as discussed in the literature [51,52]. Briefly, 3.0 g graphite flakes and 1.5 g $NaNO_3$ were mixed in the 98 wt% H_2SO_4 of 69 ml, followed by cooling to 0 °C in an ice-water bath. Next, 9.0 g $KMnO_4$ was slowly added, and the reaction was kept at 35 °C with stirring for 30 min. Upon slow addition of 138 ml water, the reaction temperature was maintained at 98 °C for 30 min. After removing the heating, the reaction was cooled down using a water bath for 10 min. After adding additional water, 3 ml H_2O_2 was slowly added. Filtering the suspension followed by sequential rinsing with 10 wt% HCl aqueous solution and deionized (DI) water removed ion species. The final sediment was dialyzed with DI water until the pH of the water became neutral. The dialyzed suspension was then centrifuged at 10,000 rpm with GO remaining in the supernatant. Finally, the samples were sonicated to yield a solution of exfoliated GO.

The rGO dispersion was prepared by the thermal reduction method. The well-exfoliated GO solution was first transferred to an autoclave and loaded into an oven. The temperature of the oven was maintained at 200 °C for 16 h. Next, removing the autoclave from the oven rapidly cooled down the solution to room temperature and terminated the reaction. The obtained rGO sheets were sonicated and stored before further processing.

2.2. Synthesis of MoS_2@rGO composite

The MoS_2@rGO composites were prepared by a solvothermal method. In brief, 24 mg MoO_3, 28 mg thioacetamide, and 0.2 g urea were dissolved in 16 ml ethanol with continuous magnetic stirring

Table 1
Performance comparison of representative NO_2 gas sensors.

Materials	Demonstrated LOD (ppb)	Operating temperature (C)	Sensitivity	Calculated LOD (ppb)	Response/ recovery time	Sensing Mechanism	Interference gases used for selectivity	Wearable device	Ref
rGO/Cu_2O	400	150	33.9%/ 1 ppm	82	5 min/12 min	CR	–	No	[33]
Black phosphorus	4	–	10%/10 ppb	–	6 min/40 min	FET	–	No	[34]
SnO_2/ZnO	1000	25 (sense) UV light (recover)	238%/ 1 ppm	–	3 min/5 min	CR	–	No	[35]
Graphene/MoS_2	50	200	7%/0.5 ppm	–	2.5 min/ 2.5 min	FET	H_2, CO	No	[28]
Ni	1000	25 (sense) 200 (recover)	1%/1 ppm	–	83 s/20 s	FET	–	No	[36]
Sulfonated Graphene	1000	25	25%/1 ppm	70	>10 min/ >20 min	EC	NH_3, H_2O, Toluene	No	[37]
Graphene	1000	25	5%/1 ppm	6.87	>15 min/ >30 min	CR	NH_3, H_2O, C_2H_5OH, $(CH_3)_2CO$	Flexible	[8]
phosphorene	20	25	150,000%/ 100 ppb	–	10 min/30 min	FET	CO, H_2S, H_2	No	[38]
PbS quantum dots	500	25	350%/ 50 ppm	84	4 s/52 s	CR	SO_2, NO, H2S, NH_3	Flexible	[39]
CVD MoS_2	5000	25 + UV light	17%/5 ppm	–	29 s/350 s	CR	NH_3, H_2, H_2S, CO_2, CH_4	NO	[29]
rGO	500	25	0.5%/ 0.5 ppm	0.4	4 min/4 min	CR	NH_3, Cl_2, CH_2Cl_2, CH_3OH, C_2H_5OH, $C_6H_5OH_3$, C_6H_{14}	Flexible	[40]
MoS_2/Pt/rGO	500	25	6%/0.5 ppm	2	1 h/>1 h	FET	–	Flexible	[17]
ZnO nanorods	1000	200–225	750%/ 10 ppm	2500	2 min/2.5 min	CR	–	No	[41]
Vertical aligned MoS_2/SiO_2	1000	100	16.2%/ 1 ppm	2.3	15 min/45 min	CR	NH_3, $(CH_3)_2CO$	No	[42]
Al doped ZnO	10,000	25	12%/ 100 ppm	–	20 min/60 min	CR	CO, NH_3	No	[43]
rGO/Fe_2O_3	50	25	90%/5 ppm	–	15 min/45 min	CR	H_2, H_2S, Cl_2, SO_2, NH_3, Benzene, Toluene	No	[44]
rGO/PEDOT	5000	80	12.5%/ 5 ppm	–	50 min/50 min	CR	NH_3, H_2S, SO_2	No	[45]
WO_3/YSZ	60	500	77mV/ 1 ppm	–	50 s/100 s	EC cell	NO, CO_2, CO, NH_3	No	[46]
NiO/YSZ	3000	850	40mV/ 100 ppm	–	25 s/50 s	EC cell	NO, NH_3, C_2H_2, CH_4, CO, H_2	No	[47]
SnS_2	600	120	3633%/ 10 ppm	20	170 s/140 s	CR	H_2, CH_4, CO_2, H_2S	No	[48]
TIPS-petacene	300	25	0.2μA/ 0.3 ppm	20	200 s/400 s	CR	SO_2, H_2O, NH_3	No	[49]
rGO/Co_3O_4	50	25	3%/50 ppb	–	5 min/40 min	CR	H_2, H_2S, NH_3, SO_2, Cl_2, $(CH_3)_2CO$, C_2H_5OH, Benzene, Toluene	No	[50]
$MoSe_2$	1000	25	100%/ 10 ppm	–	250 s/150 s	FET	NH_3, H_2S	Flexible, Stretchable	[11]
MoS_2@rGO	10	25	6%/1 ppm	4.4	6 min/12 min	CR	SO_2, CO, NH_3, NO, C_2H_5OH, $(CH_3)_2CO$	Flexible, Stretchable	This work*

CR: chemiresistor; EC: electrochemical. Note: *A static gas sensing characterization system has been used in the current study. In contrast, most of the literature reports have exploited a dynamic flow gas testing setup, which generally yields faster response/recovery processes from the flow in a much smaller chamber.

for 1 h, followed by adding 4 ml GO suspension of 3.5 mg/ml. Next, the well-mixed solution was transferred to an autoclave and loaded into a furnace (MTI). Heating the furnace to 200 °C and then the temperature was maintained for 16 h. Removing the autoclave from the oven rapidly cooled down the solution to room temperature and terminated the reaction. The as-prepared MoS_2@rGO composite was collected and washed with deionized water and then ethanol, followed by storage in the mixture of deionized water and ethanol at the volume ratio of 1:1 before use.

The confined growth of the MoS_2@rGO composites followed the same recipe as above. 12 mg MoO_3, 14 mg thioacetamide, and 0.1 g urea were dissolved in 8 ml ethanol with continuous magnetic stirring for 1 h, followed by adding 2 ml GO suspension of 3.5 mg/ml. After transferring the 10 ml reactant suspension into the autoclave reactor, 20 ml NaCl crystal fillers (Morton Salt, as-bought or ball-milled) were added into the reactor slowly with agitation. After the reactor was placed still for 5 min, the supernatant liquid was removed (the liquid existed only between the crystal fillers). After maintaining the temperature at 200 °C for 16 h, the as-prepared MoS_2@rGO filled in the confined spaces formed by crystal fillers. The crystal fillers were dissolved by water to collect the products, and the obtained products were washed by deionized water for at least five times. Finally, the black dispersive MoS_2@rGO product was dialyzed with deionized water for at least seven days using regenerated cellulose dialysis membranes until no smell.

2.3. *Raman spectroscopy*

Raman spectroscopy was carried out on a LabRam HR800 UV NIR with 532 nm laser excitation.

2.4. *SEM imaging*

The morphologies of the as-prepared MoS_2@rGO were characterized by the SEM (Hitachi S4800) at an accelerating voltage of 10.0 kV.

2.5. Surface area measurement of MoS_2@rGO composite

UV–vis spectroscopy with methylene blue (MB) dye as the probe was used so as to measure the surface area of the MoS_2@rGO composite [53]. Six different concentrations of MB aqueous solution (0.5, 1, 2, 3, 4, and 5 mg/L) were used to first obtain the standard plot. Next, 5.0 mg MoS_2@rGO sample was added into 10 mL MB solution with a concentration of 10 mg/L, followed by magnetic stirring in darkness for 24 h. Finally, the MoS_2@rGO mixtures were filtrated to collect the filter liquor for the measurement of the MB concentration. In this measurement, all the MB molecules were assumed to be flat, and the surface area of 1.30 nm^2 per molecule of MB [54] was used to calculate the surface area.

2.6. Fabrication of MoS_2@rGO-based gas sensors

The IDE was first created on thin cover glass (globe SCIENTIFIC INC) by depositing metals through a polyimide (PI) shadow mask patterned by a CO_2 laser. The PI tape (Kapton 3M) was laminated on the cover glass with its adhesive layer bonded to the glass. After patterning with a CO_2 laser (Universal Laser Systems), removal of the carbon residue from the laser processing completed the shadow mask. Electron beam (e-beam) evaporation (Semicore) of 10 nm Cr and 100 nm Au, followed by peeling off the PI shadow mask, yielded the IDE on the cover glass. Dropping the well-dispersed MoS_2@rGO suspension onto the IDE and connecting the IDE to the source meter (Keithley 2401) through copper film and silver epoxy paste (MG chemicals 8331) completed the fabrication process of the gas sensor. A Ti heater was also fabricated by following the same shadow mask deposition approach. Integrating the heater beneath the IDE with scotch tape allowed us to investigate the temperature effect on the performance of the MoS_2@rGO gas sensor.

2.7. Fabrication of stretchable MoS_2@rGO based gas sensor

The IDEs were designed to have five fingers with a width of 350 μm spaced by 200 or 80 μm to ensure good sensitivity [55]. Fabrication of the IDE was carried out by the metal evaporation through a shadow mask or by a UV laser cutting (Suzhou Tianhong Laser Co., Ltd). Briefly, 5 nm Cr as an adhesive layer and 100 nm Au as the electrode were first deposited on an ultrathin polyimide film of 8 μm (CS Hyde Company). Spin-coating a thin layer of soft polydimethylsiloxane (PDMS) (mixing ratio of 10:1) on a 6-inch Si wafer served as a temporary substrate to bond the ultrathin polyimide film. Laminating the polyimide film on PDMS (with the Au layer facing down) yielded a flat surface for the UV laser cutting. Coating a cover glass with a thin layer of a softer PDMS (mixing ratio of 20:1) by doctor blade served as the receiver substrate. Pressing the cover glass against the patterned polyimide film on the Si wafer, followed by lifting, transferred the patterned polyimide film from the Si wafer onto the cover glass with the Au electrode facing outside. The successful transfer was enabled by the difference in adhesion (i.e., the softer PDMS with a stronger adhesion to the polyimide film). Bonding the cover glass to a strip of Ecoflex (Smooth-on) with a thickness of 2 mm through a thin layer of uncured Ecoflex yielded the IDE on a stretchable substrate. Finally, the serpentine conductive ribbons patterned by the UV laser were used to connect the IDE to two contact pads, which were subsequently connected to a source meter through alligator clamps and silver epoxy.

3. Results and discussion

3.1. Synthesis and characterization of MoS_2@rGO composite

By using NaCl salt crystals with different sizes as the space filler to constrain the growth of MoS_2@rGO, the MoS_2@rGO composites with controlled morphologies were synthesized following an ethanol-thermal method (Fig. 1a). In brief, molybdenum oxide (MoO_3), thioacetamide (TAA), urea, and GO were used as the precursor for growing MoS_2 on rGO by the ethanol-thermal method. Being stable in ethanol [56], a large quantity of NaCl crystal fillers added to ethanol was able to thoroughly disperse the small number of reactant suspension (i.e., MoO_3, TAA, urea, and GO). As a result, the reactant suspension existed only in the interspaces between the NaCl crystal fillers. After solvothermal reaction, the size-regulated MoS_2@rGO composites between the NaCl crystal fillers were harvested by dissolving the NaCl with water. Controlling the confined space between NaCl crystal fillers with different crystal dimensions yielded the MoS_2@rGO composite samples with various sizes. By using ball milling with different parameters, three different sizes of NaCl crystal fillers were prepared. We denote the as-received NaCl crystal as fillers, the NaCl crystal ball milled at 300 rpm for 5 min as fine fillers, and the NaCl crystal ball milled at 400 rpm for 10 min as ultrafine fillers. Following the same approach but without the use of NaCl in the precursor, pristine MoS_2@rGO samples were obtained as the control.

The morphologies of the as-prepared rGO, MoS_2, and MoS_2@rGO samples were characterized by the scanning electron microscopy (SEM) (Fig. 1 and Fig. S1). The MoS_2@rGO composite showed a rough surface because of the interlaced MoS_2 flakes. The change from a granular-like shape to a uniform flake-like structure in MoS_2 was likely due to the presence of rGO in the composite. By ball milling the as-bought NaCl crystals into different sizes (Fig. S2), the confined space monotonically decreased in the following four samples: (1) MoS_2@rGO synthesized without NaCl crystal fillers (MoS_2@rGO without fillers, MoS_2@rGO (Fig. 1b), (2) MoS_2@rGO synthesized with as-bought NaCl crystal fillers (MoS_2@rGO with commercial fillers, C-MoS_2@rGO) (Fig. 1c), (3) MoS_2@rGO synthesized with NaCl crystal fillers ball milled at 300 rpm for 5 min (MoS_2@rGO with fine fillers, F-MoS_2@rGO) (Fig. 1d), and (4) MoS_2@rGO synthesized with NaCl crystal fillers ball milled at 400 rpm for 10 min (MoS_2@rGO with ultrafine fillers, UF-MoS_2@rGO) (Fig. 1e). As confirmed by the SEM images (Fig. 1c–e), the MoS_2@rGO samples became more uniform with reduced feature size as the confined space decreased. Forming flakes on the interconnected rGO framework, MoS_2 not only enhanced the charge transport pathway but also increased the specific surface area of the composite from 217.34 m^2/g to 283.72 m^2/g.

Raman spectroscopy analysis was further carried out to provide the structural information of the rGO, MoS_2, and MoS_2@rGO composites. The pristine rGO sample exhibited two peaks at 1350.6 and 1590.2 cm^{-1} (Fig. 2a), corresponding to the D band and G band of carbon. According to the intensity ratio of the D to G band, the degree of graphitic disordering Id/Ig was determined to be 1.09 in rGO. As shown in Fig. 2b, the pristine MoS_2 displayed four dominant peaks at 150.2, 285.3, 327.8, and 410.5 cm^{-1}, corresponding to the characteristic peaks of the phonon mode of MoS_2 [53]. Compared with the pristine MoS_2, the MoS_2 peaks in the MoS_2@rGO composites [57] (Fig. 2c–f) became weak but still existed, indicating the existence of MoS_2 in the composites. Also, two distinct peaks at 1351.5 cm^{-1} (D band) and 1590.6 cm^{-1} (G band) in the region of higher wavenumbers (1200-1800 cm^{-1}) confirmed the presence of rGO in the MoS_2@rGO composites. Using the relative intensity ratio of Id/Ig as a convenient measurement of the reduction extent in carbon materials [58], the MoS_2@rGO composites with a calculated Id/Ig value of ~1.17 indicated that the GO was reduced to a great extent in the solvothermal process [86]. The results from the above Raman spectroscopy analyses confirmed the concomitant presence of rGO and MoS_2 in the MoS_2@rGO composites.

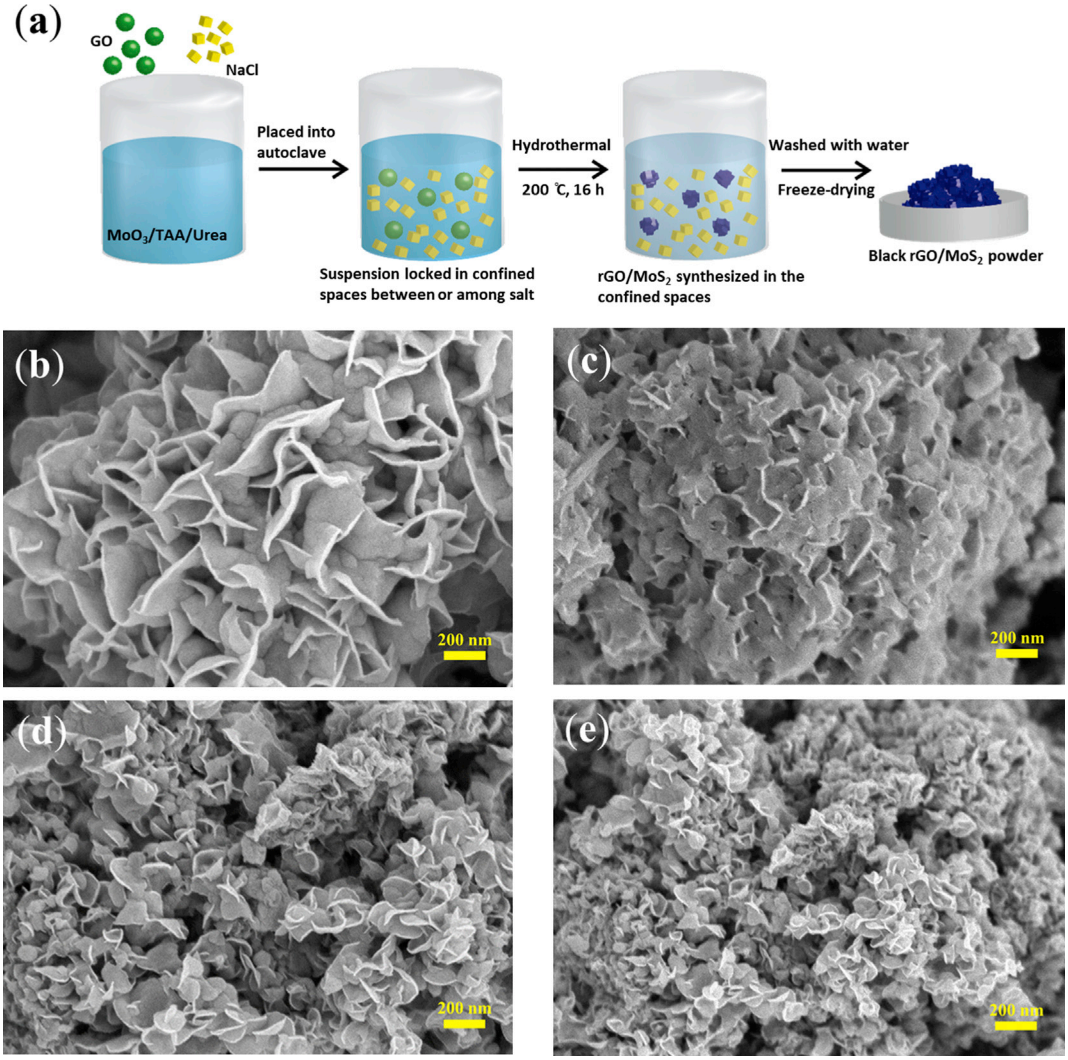

Fig. 1. MoS$_2$@rGO composites prepared by a solvothermal method with confined growth space and their corresponding SEM images. (a) Schematic of the synthesis process of the MoS$_2$@rGO samples with different surface morphologies. The surface morphology of the sample was controlled by changing the size of the confined space in the solvothermal process. SEM images of (b) MoS$_2$@rGO synthesized without adding NaCl salt crystals (MoS$_2$@rGO without fillers, MoS$_2$@rGO), (c) MoS$_2$@rGO synthesized with adding as-received NaCl salt crystals (MoS$_2$@rGO with fillers, C-MoS$_2$@rGO), (d) MoS$_2$@rGO synthesized with adding NaCl salt crystals ball milled at 300 rpm for 5 min (MoS$_2$@rGO with fine fillers, F-MoS$_2$@rGO), and (e) MoS$_2$@rGO synthesized with adding of NaCl salt crystals ball milled at 400 rpm for 10 min (MoS$_2$@rGO with ultrafine fillers, UF-MoS$_2$@rGO).

3.2. *Gas sensing performance of MoS$_2$@rGO composite*

The NO$_2$ gas sensing performance of the synthesized MoS$_2$@rGO composite was evaluated by drop-casting the suspension of the composite onto an IDE that was prepared by depositing metals through a polyimide (PI) shadow mask patterned by a CO$_2$ laser (Fig. S3). The gas-sensing performance of the MoS$_2$@rGO-based gas sensors was evaluated in a static gas sensing characterization system (Fig. S4) at both room temperature (Fig. 3) and elevated temperature (Fig. S5) that has a sealed chamber with a volume of 10 L. Because a response time of 500 s is sufficient to capture the gas sensor characteristics, this value is used in the subsequent tests for rapid testing unless otherwise specified. Increasing the working temperature of the gas sensor can also lead to an enhanced response rate. It should be noted that the testing results obtained by a dynamic flow gas testing setup would generally improve (e.g., faster response/recover processes) over those obtained by a static gas sensing characterization system, their results may not be directly applicable to the practical applications. While the temperature affects the performance of chemiresistive gas sensors (Fig. S5), the variation in the temperature on the human skin is relatively small, which would result in a small effect on the wearable gas sensor. When the temperature-induced resistance change cannot be ignored, the concept from the electronic nose can be explored to deconvolute the gas response in the presence of temperature [59]. Different concentrations of NO$_2$ in the sealed chamber were prepared by diluting the 100 ppm NO$_2$ calibration gas (GASCO) and well mixing with the air in the chamber. The operation temperature of the MoS$_2$@rGO-based gas sensors was well controlled by a heater element underneath the sensing platform. As the temperature from the Joule heating increased linearly with the increasing input power (Fig. S5d), the temperature effect on the performance of the MoS$_2$@rGO gas sensors was quickly evaluated. After transferring the gas sensors from the ambient air to 2 ppm NO$_2$ circumstance, notable changes in the sensor resistance were observed. Because of the dominating p-type rGO [60] and the poor conductivity of MoS$_2$, the MoS$_2$@rGO samples exhibited p-type characteristics, as noted in the decreased resistance upon NO$_2$ absorption. Compared with the physical mixing, the in situ synthesis of MoS$_2$ on rGO has much better contact between MoS$_2$ on

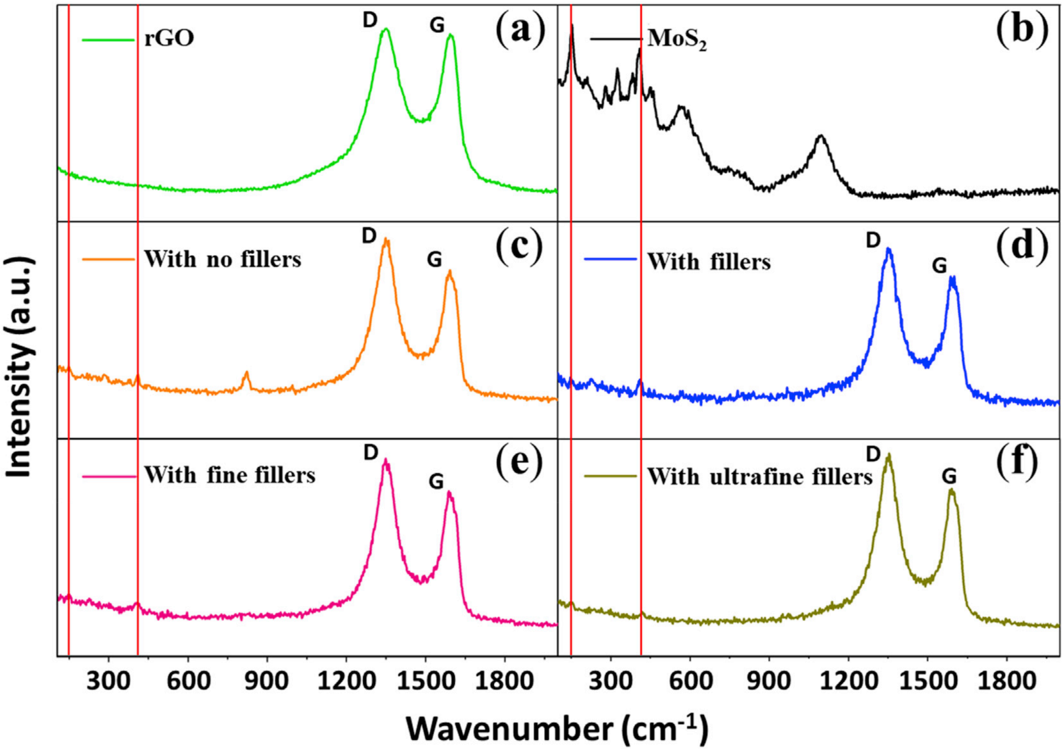

Fig. 2. **Raman spectroscopy analysis of (a)** rGO, **(b)** MoS$_2$, **(c)** MoS$_2$@rGO, **(d)** C-MoS$_2$@rGO, **(e)** F-MoS$_2$@rGO, **(f)** UF-MoS$_2$@rGO. Red lines indicated the two characteristic peaks of MoS$_2$ at 150.2 and 410.5 cm^{-1}.

rGO, which will benefit the charge transfer during device operation. Regardless of the morphologies of the MoS$_2$@rGO samples, their resistance changes all followed a similar trend that higher response and recovery rates occurred at elevated temperatures with lower sensitivity. The gas-sensing performance of various samples at room temperature was characterized (Fig. 3a). Though pristine rGO samples were capable of reversibly detecting the NO$_2$ gas at a relatively fast response/recovery rate, their responses were small (0.18%) with low sensitivity, and the considerable noise could not be used for accurate gas sensing (Fig. 3b). Because the tremendous resistance of the pristine MoS$_2$ was over the measurement range of the source meter, its gas sensing performance was not included in the comparison. Compared with the pristine rGO sample, the MoS$_2$@rGO composite without using fillers demonstrated higher sensitivity (13.7%) (Fig. 3c). The improved response was likely attributed to the enhanced charge transfer and formation of the heterojunction between rGO and MoS$_2$ [61]. By applying NaCl fillers in the synthesis process, the resulting C-MoS$_2$@rGO composite with fillers showed a further enhanced sensitivity (19.0%) (Fig. 3d). The increased sensitivity can be attributed to the increased portion of heterojunction in the bulk material as the feature size of rGO and MoS$_2$ decreases. At the interface between p-type rGO and n-type MoS$_2$, both of the hole accumulation region in rGO and the charge depletion region in MoS$_2$ extend upon NO$_2$ adsorption due to the continuous electron withdrawal. Because NO$_2$ molecules preferably adsorb onto MoS$_2$ due to its rich active sites, the rGO at the junction plays a more prominent role compared with its bulk counterpart. As the charges transfer from rGO to NO$_2$, the carrier concentration in rGO conductive paths increases to result in a resistance drop. Though the MoS$_2$@rGO samples with increased specific surface area showed a slightly decreased sensitivity that was likely due to the different ratios of MoS$_2$ in the MoS$_2$@rGO composites [61], their gas sensing measurements with a significantly reduced noise still demonstrated drastically increased SNR (i.e., the ratio of the mean value of the signal to the standard deviation of the noise [R$_0$-R]/RMS_baseline). In comparison to the SNR of 39.2 measured in the C-MoS$_2$@rGO, the SNR of the F-MoS$_2$@rGO and UF-MoS$_2$@rGO increased to 50.7 (Fig. 3e) and 60.4 (Fig. 3f), respectively. In contrast to the previous literature reports that the response/recovery processes have only been qualitatively described, the slope of the response was calculated in this study to better characterize the steady-state response conditions. As the slope of the response was calculated to be 0.154%/min at 540 s (close to plateau in Fig. 3f), it would be reasonable to assume that the sensor with a similar value in the slope of the response approximately reached the steady-state condition. Based on this consideration, a response time of 6 min was selected in the following studies unless specified otherwise. It should also be noted that a direct comparison in the response/recovery rates hinges on a standard yet quantitative description of the response/recovery processes in the literature reports. The increase in SNR was believed to result from the reduced contact impedance between the IDE and the sensing materials that were associated with reduced feature size and more uniform distribution (consistent with the observation in the improved IDE design in the next section). The significantly increased SNR enabled the sample to respond to an ultralow concentration of NO$_2$, as demonstrated in the stretchable gas sensor to be discussed in the next section. Besides, the UF-MoS$_2$@rGO also showed reasonably well repeatability in the switching cycling test between 2 ppm NO$_2$ and the air (Fig. 3g). The underlying mechanism of this outstanding recovery capability remains to be investigated, but could likely be the synergistic effect of rGO and MoS$_2$. Smaller MoS$_2$ clusters expose a higher ratio of edge sites that facilitate the adsorption of NO$_2$ molecules, leading to high sensing performance [31,62]. On the other hand, the reducing feature size leads to a more uniform contact between rGO and MoS$_2$, which facilitate the charge transfer

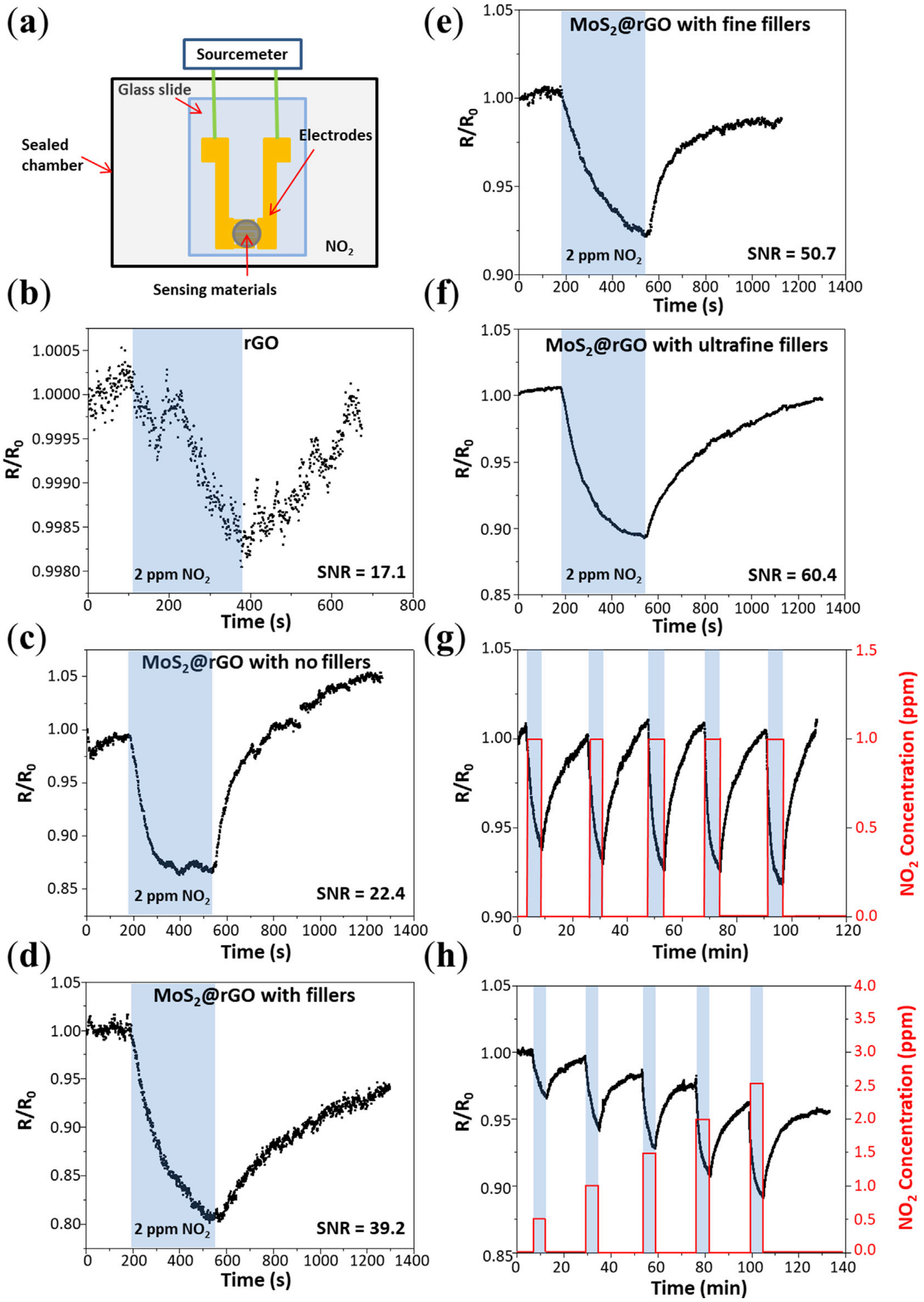

Fig. 3. NO$_2$ gas sensing performance of MoS$_2$@rGO composites. (a) Schematic illustration of the testing setup for the gas sensor, including a sealed chamber, interdigitated electrode, and a source meter (SM). Responses of five (**b**–**f**) samples to 2 ppm NO$_2$ at the room temperature. Signal to noise ratio (SNR) increased as the specific area of the MoS$_2$@rGO composite increased. (**g**) The cycle test of the UF-MoS$_2$@rGO shown in (f) to 1 ppm NO$_2$ showed reasonably good repeatability. **(h)** The calibration test of the UF-MoS$_2$@rGO shown in (f) to different concentrations of NO$_2$ demonstrated linear sensing performance.

between these two materials. The responses of the sensor to different concentrations of NO$_2$ (from 0.5 ppm to 2.5 ppm, with a step increase of 0.5 ppm) were also conducted in a continuous test (Fig. 3h). The response of the sensor increased gradually with the increasing gas concentration, indicating its robust sensing performance. The incomplete recovery presented in the dynamic curve resulted from the given short recovery time and the high-energy binding sites of rGO and MoS$_2$ [27,63].

3.3. Fabrication and characterization of stretchable NO_2 sensor

By eliminating the heater, the room temperature MoS_2@rGO based gas sensor reduces power consumption and avoids the adverse thermal effect, enabling its application toward bio-integrated electronic devices [64]. To conform to the hierarchically textured, non-developable topology of the skin surface and to deform with the natural motion of the underlying skin, the bio-integrated devices are expected to be not only flexible but also stretchable. By exploring a stretchable structure, the stretchable NO_2 gas sensor based on the MoS_2@rGO composite demonstrated the utility (Fig. 4). With a simple fabrication process (Fig. S6), the stretchable sensor was capable of conforming to hand (Fig. 4a), deforming to the fist (Fig. 4b), and being twisted (Fig. 4c) and stretched over an applied tensile strain of 20% commonly experienced on the skin surface (Fig. 4d). The small-sized glass buried between the IDE and the soft Ecoflex substrate provided the strain isolation effect (Fig. S6), which significantly reduced the strain to be negligibly small in the sensing region. Furthermore, the unfolding of the serpentine interconnects would enable them to follow the deformation applied to the sensor. To further test the hypothesis that the increased SNR was associated with reduced contact impedance between the IDE and the gas sensing materials, we reduced the spacing between the fingers of the IDE from 200 μm to 80 μm. Because of the increased conductive pathway in between fingers in the IDE, this new design further improved the SNR of the sensor (to 2 ppm NO_2) from 60.4 to 306.3 (Fig. S7) before stretching. Placing the stretchable sensor in the sealed chamber with different NO_2 concentrations from 0.5 ppm to 2.5 ppm before and after an applied tensile strain of 20% demonstrated its robust operation even upon mechanical deformation (Fig. 4e). According to the theoretical equation of the Limit of Detection (LOD) for a linear sensor: $LOD = 3 \times noise/slope$, the LOD of the stretchable gas sensor was calculated from the linearly fitted response versus NO_2 concentration curve as 4.4 ppb and 5.6 ppb before and after an applied tensile strain of 20%. The resistance of the gas sensor was monitored when a tensile strain of 20% was applied to the sensor for 100 cycles (Fig. 4f), indicating the resistance fluctuation of ~1%. The resistance fluctuation caused by 20% tensile strain is smaller than half of the sensor response to 0.5 ppm NO_2, which exhibits a much smaller influence of stretching compared to those in the literature reports [8,43,65]. No significant change of sensitivity was observed before and after the cyclic deformation (Fig. S8). The local strain in the LIG sensing region can be further reduced with enhanced strain isolation effect [66–69], pre-strain [70], or other stretchable strategies [71,72]. In the case that the strain-induced small resistance change needs to be accounted for, the concept from the electronic nose can also be applied to deconvolute the gas response from the strain [73,74]. Furthermore, the applied strain from the skin to the sensor could be much smaller than 20% if the stretchable gas sensor is placed on regions with a small strain (e.g., the middle of a human subject's forearm) [75,76]. It should be noted that the calibration curve of the stretchable gas sensor was not linear, and it had a much higher slope at a lower concentration than that at the higher concentration partially due to the saturation of NO_2 absorption on MoS_2@rGO at high concentration. Therefore, the actual LOD of the stretchable gas sensor should be much lower than the above estimations. To verify this hypothesis, we tested the sensing performance of the stretchable gas sensor at an ultralow concentration of 10 ppb at room temperature (Fig. 4g). Because of the easy absorption and desorption at the ultralow concentration, fast response and recovery were observed. Though the response was only 0.125%, the sensor still exhibited an excellent SNR of 35.4. Because the measured SNR at 10 ppb was more than 10-fold of the SNR value needed to differentiate the signal from the noise, we believe that the stretchable gas sensor could be used for the detection of NO_2 even at ppt levels. Because of the possible inaccuracy to calibrate the ppt level concentrations of NO_2 in the current testing setup, the demonstration of ppt level detection was not investigated here. The excellent selectivity of the stretchable MoS_2@rGO-based gas sensor was confirmed by comparing its response to NO_2 with those to the other common air pollutants. In the demonstration, the response of the stretchable MoS_2@rGO-based gas sensor to 2 ppm NO_2 was significantly higher than those to NO, CO, NH_3, SO_2 of 1 ppm, or acetone and ethanol of 100 ppm (Fig. 4h), highlighting the excellent selectivity. In addition to the common interfering gas species in the aforementioned discussion, humidity often dominates the response in many gas sensors reported in the literature, especially for those operating at room or low temperatures. Exposing the gas sensor from the ambient environment to the relative humidity (RH) of 90% resulted in a resistance decrease of 15%, indicating a large humidity effect (Fig. S9). However, several methods can be explored to mitigate the humidity effect. First of all, the humidity effect is significantly reduced from 15% to less than 2% when the sensor is operated at an elevated temperature of 40 °C after integrating a heater on the backside of the cover glass beneath the IDE. When the gas sensor is used in the environment with a range of different humidity levels, calibration of the gas sensor to various relative humidity levels is needed for the accurate detection of NO_2. The slightly elevated temperature is also below the tolerance threshold of the human skin of 43 °C [77]. Secondly, a zeolite layer can be coated over the gas sensor as a moisture barrier layer to minimize the humidity effect [78]. Last but not least, the algorithm from the electronic nose [73,74] could be implemented to cancel the humidity effect with measurements from two sensors, where one is subject to gas and humidity and the other is only subject to humidity. The stretchable NO_2 gas sensor was also demonstrated to be relatively stable in a long-term stability study by exposing the sensor to 2.5 ppm NO_2 every week for consecutive 6 weeks at 40 °C (Fig. S10a). The gas sensor exhibited a sensitivity of 7.1% with a small fluctuation because of the fluctuation in the relative humidity and other impurities in the ambient air environment (Fig. S10b). However, sample-to-sample variation was still observed in the stretchable gas sensors (Fig. S11), possibly caused by changes in the ambient environment during fabrication and changes in the distribution of the MoS_2@rGO on the IDEs from a less-controlled drop-casting process. These changes would cause the differences in the initial resistance of the sensor, the exposed surface area of the sensing material, and the conductive pathway between the sensing material and electrodes. These challenges before high-volume production can be addressed through future verification and validation activities, and the use of atomic layer deposition or magnetron sputtering that has a more accurate control. Nevertheless, calibration of each gas sensor can be carried out to ensure accurate reading of the NO_2 concentration before use in the presence of the response variation.

3.4. Fabrication and characterization of stretchable LIG-based NO_2 sensor

Though being widely used in the testing of gas sensing materials, the IDE with smaller spacing between fingers was demonstrated to have a higher SNR. While it is feasible to fabricate the IDE with significantly reduced spacing to further enhance the SNR, the complexity and corresponding cost associated with the fabrication of the gas sensor would become prohibitive. As an alternative, a single conductive line with an appropriate resistance would allow accurate measurement of the resistance change in the gas sensing material cast on top. Considering laser-induced graphene (LIG) [79,80] with a suitable sheet resistance of ~30 Ω/sq and an

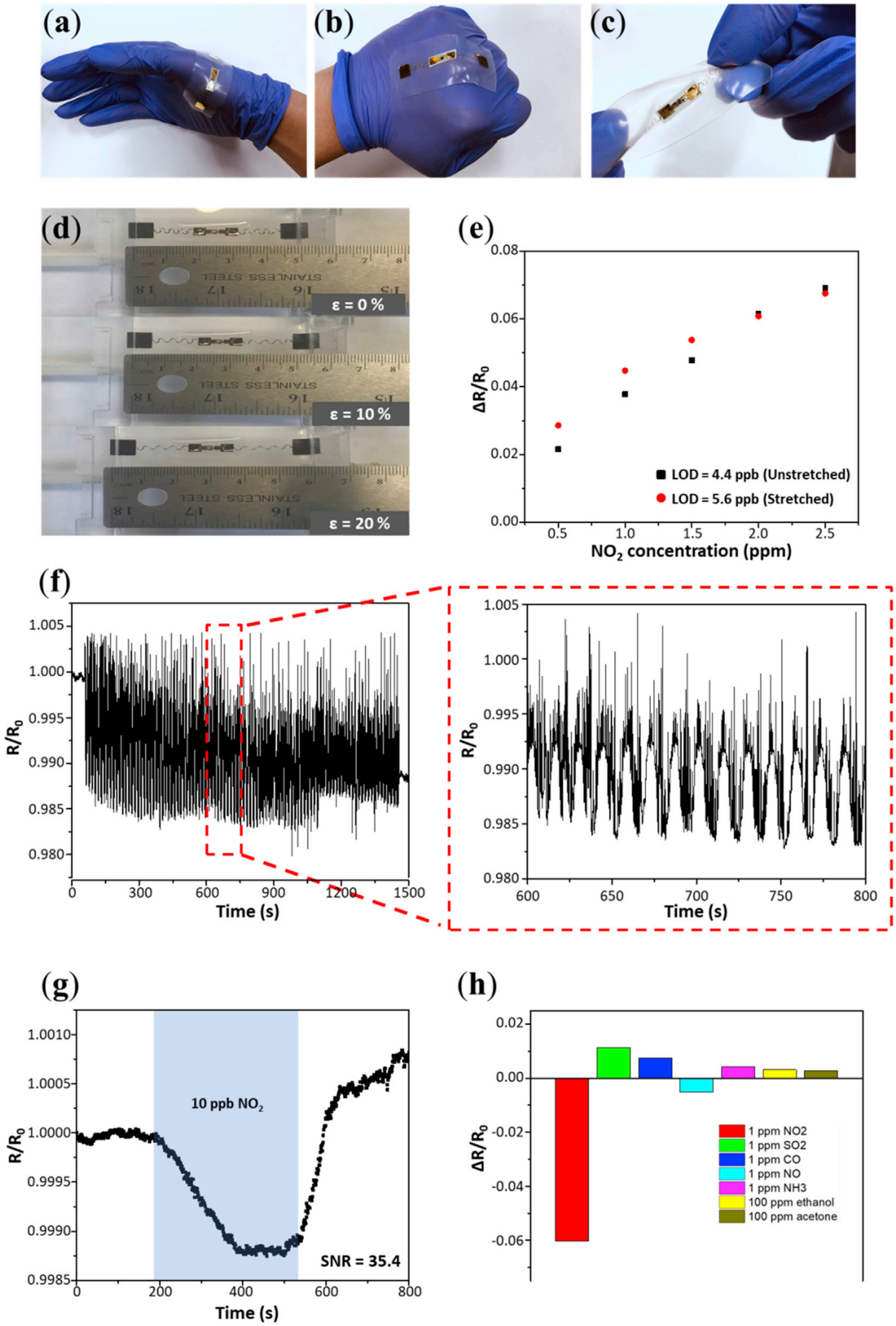

Fig. 4. Stretchable NO$_2$ gas sensor for bio-integrated electronics. (**a**–**c**) Demonstration of the stretchable gas sensor deformed by (**a**) conforming to the hand, (**b**) bending to the fist, (**c**) twisting. (**d**) Optical images of the gas sensor stretched with an applied tensile strain of 0%, 10%, and 20%. (**e**) Responses of the stretchable gas sensor to different concentrations of NO$_2$ (from 0.5 ppm to 2.5 ppm with a step size of 0.5 ppm) before and after a tensile strain of 20%. The calculated limit of detections (LOD) of the stretchable gas sensor indicated its ability to detect an ultralow concentration of NO$_2$ in ppb level or close to ppt level. (**f**) Normalized resistance change with variation in the applied strain to the gas sensor for 100 cycles. (**g**) The measurement of the gas sensor to NO$_2$ of 10 ppb demonstrated an excellent SNR of 35.4, promising the detection of NO$_2$ with ppt concentrations (Note: The gap between fingers of IDE reduced from 200 μm to 80 μm in the stretchable gas sensor). (**h**) The selectivity of the stretchable MoS$_2$@rGO gas sensor.

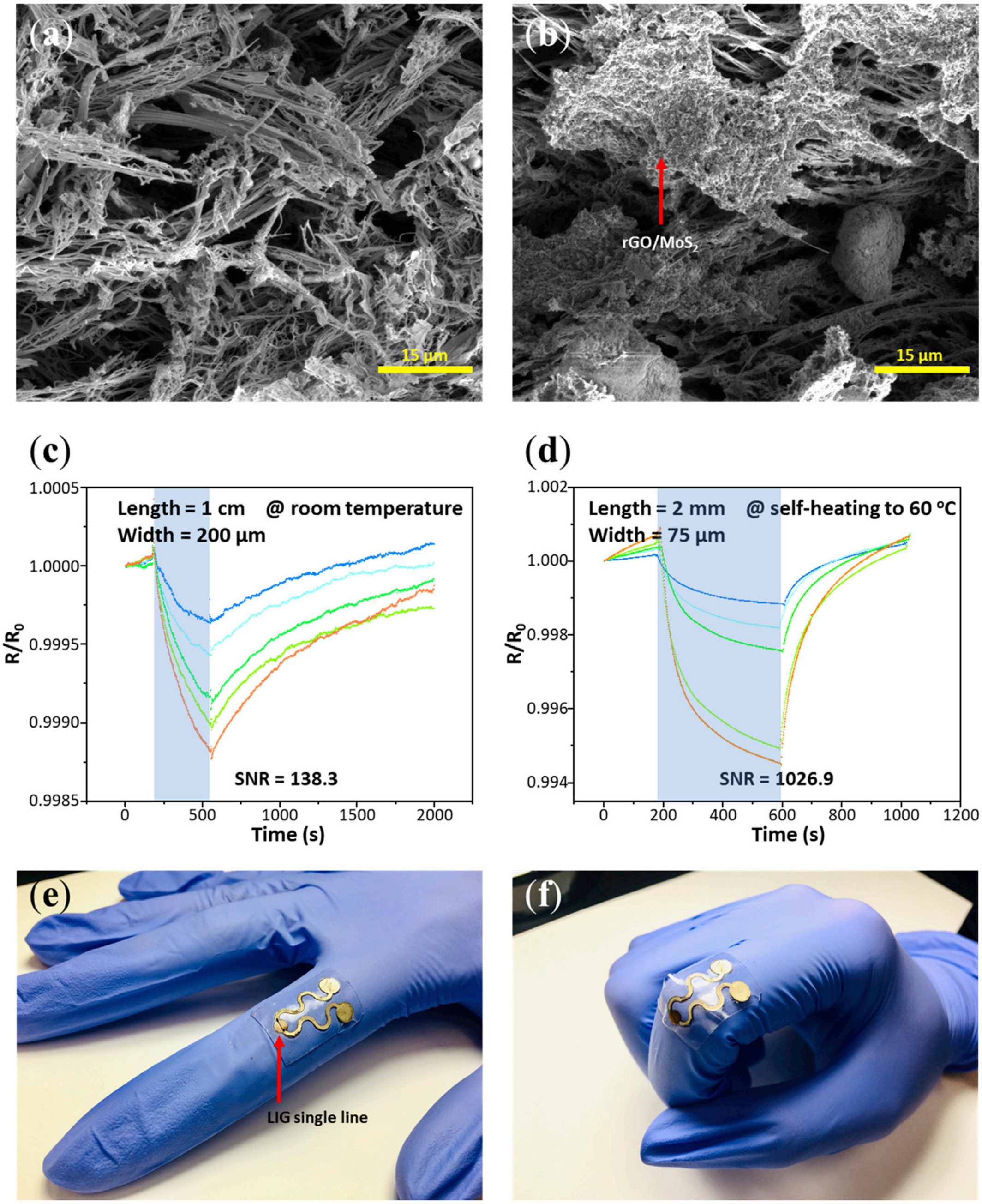

Fig. 5. Wearable MoS$_2$@rGO-based NO$_2$ gas sensor on a highly porous laser-induced graphene (LIG) conductive line. SEM images of the LIG single line on the polyimide film **(a)** before and **(b)** after casting with MoS$_2$@rGO composite. The responses of the MoS$_2$@rGO-based gas sensor on a LIG pattern to various NO$_2$ concentrations: **(c)** LIG with a length of 1 cm and a width of 200 µm at room temperature, and **(d)** LIG with a length of 2 mm and a width of 75 µm connected to wavy LIG patterns with a width of 400 µm upon self-heating to 60 °C. Optical images of wearable MoS$_2$@rGO-based NO$_2$ gas sensor on a stretchable LIG pattern **(e)** before and **(f)** after bending of the finger.

extremely large specific surface area (~350 m^2/g) [81], the 3D porous graphene material fabricated from direct laser writing on the commercial polyimide (PI) represents a promising candidate as the conductive line for gas sensing applications. To prepare the LIG-based gas sensor, we first fabricated a highly porous LIG conductive line with a width of 200 µm (Fig. 5a) and a length of 1 cm by scribing a CO$_2$ laser (Universal Laser Systems) on the commercial polyimide tape (Kapton, 75 µm thickness) with a laser power of 4% and a scanning speed of 1% on the glass. The SEM image indicates an interconnected fibrous-like porous structure for the laser-ablated PI film, exhibiting similar results as previously reported [81]. Raman spectrum of the single line showed characteristic peaks at ~1350 cm^{-1} (D peak), ~1574 cm^{-1} (G peak), and ~2700 cm^{-1} (2D peak), consistent with the previously reported values of LIG to confirm its existence (Fig. S12a) [82]. The G/2D intensity ratio in the Raman spectrum indicated the existence of multilayer (>23) graphite [83]. Casting UF-MoS$_2$@rGO onto the surface (Fig. 5b) of the LIG sensing region by a microliter pipette completed the fabrication of the gas sensor. After the initial increase, the resistance decreased to a value smaller than its initial level as the organic solvent evaporated (Fig. S12b), indicating resistors connected in parallel between the LIG and MoS$_2$@rGO sensing materials. Considering the substantially larger resistance of the MoS$_2$@rGO than that of the LIG and the significant contribution of the bare LIG line (i.e., no MoS_2@rGO coating) to the total resistance, the response of this gas sensor to 2 ppm NO_2 at room temperature was only 0.1% (Fig. 5c), as opposed to 11.0% in that of IDE. However, the gas sensor still exhibited an excellent SNR of 138.3, due to the improved contact between the MoS_2@rGO sample and highly porous LIG. To make a stretchable NO_2 sensor with self-heating capability, we further fabricate a LIG pattern with a small single line (with a reduced width of 75 μm and length of 2 mm) connected by lines with a width of 400 μm. The serpentine area was coated with silver nanoparticle ink (Novacentrix AJ-A191), followed by curing at 180 C for 10 min, to significantly reduce their resistance. The single line region was then decorated with UF-MoS_2@rGO with a resistance dominating the sensor. Such a design makes sure the overall resistance of the sensor is mainly the resistance of the LIG single line. Because of the location-dependent conductivity in the LIG pattern, the voltage applied by the source meter for the resistance measurement induced localized heating in the sensing region (60 °C in Fig. 5d) at the single line area. More importantly, the existing stiff PI beneath the LIG sensing region and wavy LIG pattern created by the simple laser scribing process would easily yield stretchable gas sensors to follow arbitrary skin motions such as bending of fingers (Fig. 5e and f). Because the PI beneath the LIG sensing region is much stiffer than the soft substrate elsewhere, the strain in the sensing region is significantly smaller than the applied value due to the strain isolation effect [84]. Although the wavy LIG region would experience a larger strain compared to the applied value, its wavy geometry could unfold to follow the deformation. The small resistance change in the wavy LIG region would also become negligible to the overall resistance due to its significantly reduced resistance value compared to the sensing region. Furthermore, the LIG is also intrinsically stretchable, with the microscopic mechanism of its stretching behavior described elsewhere [85]. The self-heating in the LIG yielded a significantly enhanced SNR of 1026.9 at 2 ppm, as well as a 5-fold increase in the response. Considering the high SNR of over 60 to NO_2 of 10 ppb [32], the new LIG gas sensing platform with a simple fabrication process is indeed very effective in testing various nanomaterials and enable stretchable gas sensors. The extraordinary SNR would further enable the detection of NO_2 with an ultralow concentration (i.e., ppt level). The elevated temperature also facilitated fast response and recovery (e.g., a shorter recovery time of 400 s as opposed to > 1500 s). The LIG sensing region can also be decorated with other gas-sensitive nanomaterials either before or after the laser ablation process. The novel LIG-based gas sensing platform will enable the integration and testing of various nanomaterials through a simple fabrication process to conveniently yield chemiresistive gas sensors, which can detect various target gas species for health monitoring.

4. Conclusion

By adding NaCl crystal fillers with various sizes for the confined growth of MoS_2@rGO composites in a simple solvothermal method, we synthesized the MoS_2@rGO gas sensing material with a controlled specific surface area. The synthesized MoS_2@rGO composites became more uniform with reduced feature size and increased specific surface area as the confined space reduced. Integrating the resulting MoS_2@rGO composites on an IDE yielded chemiresistive NO_2 sensors. Characterization of the MoS_2@rGO-based gas sensor demonstrated room temperature sensing capability and the MoS_2@rGO samples with the increased specific surface area also exhibited significantly improved sensing performance in terms of the fast response/recovery, good selectivity, and drastically enhanced SNR for detection of NO_2 with ultralow concentrations. The MoS_2@rGO-based NO_2 gas sensor designed in a stretchable form demonstrated its utility as a stretchable gas sensor toward bio-integrated devices. The sensing performance of the stretchable gas sensor was evaluated before and after the applied tensile strain, confirming its robust operation upon mechanical deformation. Additionally, the IDE design with reduced spacing between fingers created by a simple laser cutting process further increased the SNR to 306.3 at a NO_2 concentration of 2 ppm. Capable of detecting NO_2 with a concentration of 10 ppb with an SNR of 35.4 and fast response/recovery, the stretchable gas sensor enabled the detection of an ultralow concentration to be even in the ppt level. In contrast to the above stretchable gas sensors that rely on the use of IDEs, the novel gas sensing platform that is based on a stretchable 3D porous LIG pattern significantly simplifies the fabrication process of the sensors. With the 3D highly porous and interconnected fibrous network structure, the LIG exhibits a high specific surface area and improved contact with the gas-sensitive nanomaterials. When combined with synthesized ultra-fine MoS_2@rGO, the resulting stretchable gas sensor exhibited an extraordinary SNR of 1026.9 to NO_2 of 2 ppm and >60 to 10 ppb.

Author Contributions

Ning Yi: Data curation; Formal analysis; Investigation; Writing-original draft

Zheng Cheng: Materials synthesis; Data curation; Formal analysis; Investigation; Writing-editing

Han Li: Methodology; Data curation; Investigation; Writing-review

Li Yang; Data curation

Jia Zhu: Validation

Xiaoqi Zheng: Data curation

Yong Chen; Visualization

Zhendong Liu: Investigation

Hongli Zhu: Resources; Supervision; Project administration; Writing-review

Huanyu Cheng: Resources; Supervision; Project administration; Writing-review

Notes

One or more provisional patents are being filed on this work.

Declaration of competing interest

The authors declare that they have no known competing financial interests or personal relationships that could have appeared to influence the work reported in this paper.

Acknowledgment

N.Y. and H.C. would like to thank Donghai Qiu and Senhao Zhang for their help with the UV laser cutting experiments. J.Z. would like to thank the support from the Leihton Riess Graduate Fellowship in Engineering. The helpful editing of the manuscript from Mr. Antonino LoVerso is also acknowledged. This research is supported by the start-up fund at The Pennsylvania State University and National Science Foundation (NSF) (Grant No. ECCS-1933072) to H.C., and the start-up grant at Northeastern University and Tier1 fund to H.Z. The partial support from the Materials for Enhancing Energy and Environmental Stewardship Seed Grant Program and the Commonwealth Campuses & Shared Facilities & Collaboration Development Program at Penn State, and the Doctoral New Investigator grant from the

American Chemical Society Petroleum Research Fund is also acknowledged.

Appendix A. Supplementary data

Supplementary data to this article can be found online at https://doi.org/10.1016/j.mtphys.2020.100265.

References

[1] G. Weinmayr, E. Romeo, M. De Sario, S.K. Weiland, F. Forastiere, Short-term effects of PM10 and NO2 on respiratory health among children with asthma or asthma-like symptoms: a systematic review and meta-analysis, Environ. Health Perspect. 118 (2009) 449.

[2] J. Kong, N. Franklin, C. Zhou, M. Chapline, S. Peng, K. Cho, H. Dai, Science (2000) 622, https://doi.org/10.1126/science.287.5453.622 287. Google Scholar Crossref, CAS (1801).

[3] G. Ko, H.-Y. Kim, J. Ahn, Y.-M. Park, K.-Y. Lee, J. Kim, Graphene-based nitrogen dioxide gas sensors, Curr. Appl. Phys. 10 (2010) 1002.

[4] G.D. Clayton, F.E. Clayton, Patty's Industrial Hygiene and Toxicology. Vol. 2A. Toxicology, John Wiley & Sons, Inc., Baffins Lane, Chichester, Sussex PO19 1DU, 1981.

[5] N.R. Council, Emergency and Continuous Exposure Guidance Levels for Selected Submarine Contaminants, National Academies Press, 2008.

[6] R.D. Brook, S. Rajagopalan, C.A. Pope III, J.R. Brook, A. Bhatnagar, A.V. Diez-Roux, F. Holguin, Y. Hong, R.V. Luepker, M.A. Mittleman, Particulate matter air pollution and cardiovascular disease: an update to the scientific statement from the American Heart Association, Circulation 121 (2010) 2331.

[7] P.L. Ljungman, N. Berglind, C. Holmgren, F. Gadler, N. Edvardsson, G. Pershagen, M. Rosenqvist, B. Sjögren, T. Bellander, Rapid effects of air pollution on ventricular arrhythmias, Eur. Heart J. 29 (2008) 2894.

[8] Y.H. Kim, S.J. Kim, Y.-J. Kim, Y.-S. Shim, S.Y. Kim, B.H. Hong, H.W. Jang, Self-activated transparent all-graphene gas sensor with endurance to humidity and mechanical bending, ACS Nano 9 (2015) 10453.

[9] J.R. Stetter, J. Li, Amperometric gas sensors a review, Chem. Rev. 108 (2008) 352.

[10] R. Baron, J. Saffell, Amperometric gas sensors as a low cost emerging technology platform for air quality monitoring applications: a review, ACS Sens. 2 (2017) 1553.

[11] S. Guo, D. Yang, S. Zhang, Q. Dong, B. Li, N. Tran, Z. Li, Y. Xiong, M.E. Zaghloul, Development of a cloud-based epidermal MoSe2 device for hazardous gas sensing, Adv. Funct. Mater. (2019) 1900138.

[12] H. Li, W. Xie, B. Liu, C. Wang, Y. Wang, X. Duan, Q. Li, T. Wang, Gas modulating effect in room temperature ammonia sensing, Sensor. Actuator. B Chem. 242 (2017) 404.

[13] N. Joshi, T. Hayasaka, Y. Liu, H. Liu, O.N. Oliveira, L. Lin, A review on chemiresistive room temperature gas sensors based on metal oxide nanostructures, graphene and 2D transition metal dichalcogenides, Microchim. Acta 185 (2018) 213.

[14] G. Korotcenkov, Gas response control through structural and chemical modification of metal oxide films: state of the art and approaches, Sensor. Actuator. B Chem. 107 (2005) 209.

[15] Q. He, S. Wu, Z. Yin, H. Zhang, Graphene-based electronic sensors, Chem. Sci. 3 (2012) 1764.

[16] S. Yang, C. Jiang, S.-h. Wei, Gas sensing in 2D materials, Appl. Phys. Rev. 4 (2017): 021304.

[17] Q. He, Z. Zeng, Z. Yin, H. Li, S. Wu, X. Huang, H. Zhang, Fabrication of flexible MoS2 thin-film transistor arrays for practical gas-sensing applications, Small 8 (2012) 2994.

[18] W. Park, J. Park, J. Jang, H. Lee, H. Jeong, K. Cho, S. Hong, T. Lee, Oxygen environmental and passivation effects on molybdenum disulfide field effect transistors, Nanotechnology 24 (2013): 095202.

[19] H. Qiu, L. Pan, Z. Yao, J. Li, Y. Shi, X. Wang, Electrical characterization of back-gated bi-layer MoS2 field-effect transistors and the effect of ambient on their performances, Appl. Phys. Lett. 100 (2012) 123104.

[20] S. Cui, Z. Wen, X. Huang, J. Chang, J. Chen, Stabilizing MoS2 nanosheets through SnO2 nanocrystal decoration for high-performance gas sensing in air, Small 11 (2015) 2305.

[21] D. Zhang, C. Jiang, P. Li, Y.e. Sun, Layer-by-layer self-assembly of Co3O4 nanorod-decorated MoS2 nanosheet-based nanocomposite toward high-performance ammonia detection, ACS Appl. Mater. Interfaces 9 (2017) 6462.

[22] Y. Han, D. Huang, Y. Ma, G. He, J. Hu, J. Zhang, N. Hu, Y. Su, Z. Zhou, Y. Zhang, Design of hetero-nanostructures on MoS2 nanosheets to boost NO2 room-temperature sensing, ACS Appl. Mater. Interfaces 10 (2018) 22640.

[23] B. Cho, J. Yoon, S.K. Lim, A.R. Kim, D.-H. Kim, S.-G. Park, J.-D. Kwon, Y.-J. Lee, K.-H. Lee, B.H. Lee, Chemical sensing of 2D graphene/MoS2 heterostructure device, ACS Appl. Mater. Interfaces 7 (2015) 16775.

[24] F. Schedin, A. Geim, S. Morozov, E. Hill, P. Blake, M. Katsnelson, K. Novoselov, Detection of individual gas molecules adsorbed on graphene, Nat. Mater. 6 (2007) 652.

[25] R.K. Paul, S. Badhulika, N.M. Saucedo, A. Mulchandani, Graphene nanomesh as highly sensitive chemiresistor gas sensor, Anal. Chem. 84 (2012) 8171.

[26] M.W. Nomani, R. Shishir, M. Qazi, D. Diwan, V. Shields, M. Spencer, G.S. Tompa, N.M. Sbrockey, G. Koley, Highly sensitive and selective detection of NO2 using epitaxial graphene on 6H-SiC, Sensor. Actuator. B Chem. 150 (2010) 301.

[27] G. Lu, S. Park, K. Yu, R.S. Ruoff, L.E. Ocola, D. Rosenmann, J. Chen, Toward practical gas sensing with highly reduced graphene oxide: a new signal processing method to circumvent run-to-run and device-to-device variations, ACS Nano 5 (2011) 1154.

[28] H. Long, A. Harley-Trochimczyk, T. Pham, Z. Tang, T. Shi, A. Zettl, C. Carraro, M.A. Worsley, R. Maboudian, High surface area MoS2/graphene hybrid aerogel for ultrasensitive NO2 detection, Adv. Funct. Mater. 26 (2016) 5158.

[29] R. Kumar, N. Goel, M. Kumar, UV-activated MoS2 based fast and reversible NO2 sensor at room temperature, ACS Sens. 2 (2017) 1744.

[30] Y.R. Choi, Y.-G. Yoon, K.S. Choi, J.H. Kang, Y.-S. Shim, Y.H. Kim, H.J. Chang, J.-H. Lee, C.R. Park, S.Y. Kim, Role of oxygen functional groups in graphene oxide for reversible room-temperature NO2 sensing, Carbon 91 (2015) 178.

[31] S.-Y. Cho, S.J. Kim, Y. Lee, J.-S. Kim, W.-B. Jung, H.-W. Yoo, J. Kim, H.-T. Jung, Highly enhanced gas adsorption properties in vertically aligned MoS2 layers, ACS Nano 9 (2015) 9314.

[32] L. Yang, N. Yi, J. Zhu, Z. Cheng, X. Yin, X. Zhang, H. Zhu, H. Cheng, Novel gas sensing platform based on a stretchable laser-induced graphene pattern with self-heating capabilities, J. Mater. Chem. A 8 (2020) 6487.

[33] S. Deng, V. Tjoa, H.M. Fan, H.R. Tan, D.C. Sayle, M. Olivo, S. Mhaisalkar, J. Wei, C.H. Sow, Reduced graphene oxide conjugated Cu2O nanowire mesocrystals for high-performance NO2 gas sensor, J. Am. Chem. Soc. 134 (2012) 4905.

[34] A.N. Abbas, B. Liu, L. Chen, Y. Ma, S. Cong, N. Aroonyadet, M. Köpf, T. Nilges, C. Zhou, Black phosphorus gas sensors, ACS Nano 9 (2015) 5618.

[35] S. Park, S. An, Y. Mun, C. Lee, UV-enhanced NO2 gas sensing properties of SnO2-core/ZnO-shell nanowires at room temperature, ACS Appl. Mater. Interfaces 5 (2013) 4285.

[36] H.M. Fahad, H. Shiraki, M. Amani, C. Zhang, V.S. Hebbar, W. Gao, H. Ota, M. Hettick, D. Kiriya, Y.-Z. Chen, Room temperature multiplexed gas sensing using chemical-sensitive 3.5-nm-thin silicon transistors, Sci. Adv. 3 (2017): e1602557.

[37] W. Yuan, A. Liu, L. Huang, C. Li, G. Shi, High-performance NO2 sensors based on chemically modified graphene, Adv. Mater. 25 (2013) 766.

[38] S. Cui, H. Pu, S.A. Wells, Z. Wen, S. Mao, J. Chang, M.C. Hersam, J. Chen, Ultrahigh sensitivity and layer-dependent sensing performance of phosphorene-based gas sensors, Nat. Commun. 6 (2015) 8632.

[39] H. Liu, M. Li, O. Voznyy, L. Hu, Q. Fu, D. Zhou, Z. Xia, E.H. Sargent, J. Tang, Physically flexible, rapid-response gas sensor based on colloidal quantum dot solids, Adv. Mater. 26 (2014) 2718.

[40] V. Dua, S.P. Surwade, S. Ammu, S.R. Agnihotra, S. Jain, K.E. Roberts, S. Park, R.S. Ruoff, S.K. Manohar, All-organic vapor sensor using inkjet-printed reduced graphene oxide, Angew. Chem. Int. Ed. 49 (2010) 2154.

[41] X. Wang, F. Sun, Y. Duan, Z. Yin, W. Luo, Y. Huang, J. Chen, Highly sensitive, temperature-dependent gas sensor based on hierarchical ZnO nanorod arrays, J. Mater. Chem. C 3 (2015) 11397.

[42] Y.-S. Shim, K.C. Kwon, J.M. Suh, K.S. Choi, Y.G. Song, W. Sohn, S. Choi, K. Hong, J.-M. Jeon, S.-P. Hong, Synthesis of numerous edge sites in MoS2 via SiO2 nanorods platform for highly sensitive gas sensor, ACS Appl. Mater. Interfaces 10 (2018) 31594.

[43] G. Namgung, Q.T.H. Ta, W. Yang, J.-S. Noh, Diffusion-driven Al-doping of ZnO nanorods and stretchable gas sensors made of doped ZnO nanorods/Ag nanowires bilayers, ACS Appl. Mater. Interfaces 11 (2018) 1411.

[44] B. Zhang, G. Liu, M. Cheng, Y. Gao, L. Zhao, S. Li, F. Liu, X. Yan, T. Zhang, P. Sun, The preparation of reduced graphene oxide-encapsulated α-Fe2O3 hybrid and its outstanding NO2 gas sensing properties at room temperature, Sensor. Actuator. B Chem. 261 (2018) 252.

[45] K. Dunst, D. Jurków, P. Jasiński, Laser patterned platform with PEDOT−graphene composite film for NO2 sensing, Sensor. Actuator. B Chem. 229 (2016) 155.

[46] X. Zheng, C. Zhang, J. Xia, G. Zhou, D. Jiang, S. Wang, X. Li, Y. Shen, M. Dai, B. Wang, Mesoporous tungsten oxide electrodes for YSZ-based mixed potential sensors to detect NO2 in the sub ppm-range, Sensor. Actuator. B Chem. 284 (2019) 575.

[47] R. You, X. Hao, H. Yu, B. Wang, G. Lu, F. Liu, T. Cui, High performance mixed-potential-type Zirconia-based NO2 sensor with self-organizing surface structures fabricated by low energy ion beam etching, Sensor. Actuator. B Chem. 263 (2018) 445.

[48] J.Z. Ou, W. Ge, B. Carey, T. Daeneke, A. Rotbart, W. Shan, Y. Wang, Z. Fu, A.F. Chrimes, W. Wlodarski, Physisorption-based charge transfer in two-dimensional SnS2 for selective and reversible NO2 gas sensing, ACS Nano 9 (2015) 10313.

[49] Z. Wang, L. Huang, X. Zhu, X. Zhou, L. Chi, An ultrasensitive organic semiconductor NO2 sensor based on crystalline TIPS-pentacene films, Adv. Mater. 29 (2017) 1703192.

[50] B. Zhang, M. Cheng, G. Liu, Y. Gao, L. Zhao, S. Li, Y. Wang, F. Liu, X. Liang, T. Zhang, Room temperature NO2 gas sensor based on porous Co3O4 slices/reduced graphene oxide hybrid, Sensor. Actuator. B Chem. 263 (2018) 387.

[51] D.C. Marcano, D.V. Kosynkin, J.M. Berlin, A. Sinitskii, Z. Sun, A. Slesarev, L.B. Alemany, W. Lu, J.M. Tour, Improved synthesis of graphene oxide, ACS Nano 4 (2010) 4806.

[52] L. Chen, G. Shi, J. Shen, B. Peng, B. Zhang, Y. Wang, F. Bian, J. Wang, D. Li, Z. Qian, Ion sieving in graphene oxide membranes via cationic control of

interlayer spacing, Nature 550 (2017) 380.

[53] L. Yang, A. Mukhopadhyay, Y. Jiao, J. Hamel, M. Benamara, Y. Xing, H. Zhu, Aligned and stable metallic MoS 2 on plasma-treated mass transfer channels for the hydrogen evolution reaction, J. Mater. Chem. 5 (2017) 25359.

[54] S. Zhu, X. Geng, Y. Han, M. Benamara, L. Chen, J. Li, I. Bilgin, H. Zhu, Metallic and highly conducting two-dimensional atomic arrays of sulfur enabled by molybdenum disulfide nanotemplate, Npj Comput. Mater. 3 (2017) 1.

[55] N. Mazlan, M. Ramli, M. Abdullah, D. Halin, S. Isa, L. Talip, N. Danial, S. Murad, Interdigitated electrodes as impedance and capacitance biosensors: a review, in: AIP Conference Proceedings, vol. 1885, AIP Publishing LLC, 2017: 020276.

[56] X. Xiao, H. Song, S. Lin, Y. Zhou, X. Zhan, Z. Hu, Q. Zhang, J. Sun, B. Yang, T. Li, Scalable salt-templated synthesis of two-dimensional transition metal oxides, Nat. Commun. 7 (2016) 1.

[57] A.V. Agrawal, R. Kumar, S. Venkatesan, A. Zakhidov, G. Yang, J. Bao, M. Kumar, M. Kumar, Photoactivated mixed in-plane and edge-enriched p-Type MoS2 flake-based NO2 sensor working at room temperature, ACS Sens. 3 (2018) 998.

[58] Y. Du, J. Wang, Y. Zou, W. Yao, J. Hou, L. Xia, A. Peng, A. Alsaedi, T. Hayat, X. Wang, Synthesis of molybdenum disulfide/reduced graphene oxide composites for effective removal of Pb (II) from aqueous solutions, Sci. Bull. 62 (2017) 913.

[59] J. Burgués, S. Marco, Low power operation of temperature-modulated metal oxide semiconductor gas sensors, Sensors 18 (2018) 339.

[60] G. Lu, L.E. Ocola, J. Chen, Gas detection using low-temperature reduced graphene oxide sheets, Appl. Phys. Lett. 94 (2009): 083111.

[61] Y. Zhou, G. Liu, X. Zhu, Y. Guo, Ultrasensitive NO2 gas sensing based on rGO/MoS2 nanocomposite film at low temperature, Sensor. Actuator. B Chem. 251 (2017) 280.

[62] R. Kumar, P.K. Kulriya, M. Mishra, F. Singh, G. Gupta, M. Kumar, Highly selective and reversible NO2 gas sensor using vertically aligned MoS2 flake networks, Nanotechnology 29 (2018) 464001.

[63] D.J. Late, Y.-K. Huang, B. Liu, J. Acharya, S.N. Shirodkar, J. Luo, A. Yan, D. Charles, U.V. Waghmare, V.P. Dravid, Sensing behavior of atomically thin-layered MoS2 transistors, ACS Nano 7 (2013) 4879.

[64] Z. Lim, Z. Chia, M. Kevin, A. Wong, G. Ho, A facile approach towards ZnO nanorods conductive textile for room temperature multifunctional sensors, Sensor. Actuator. B Chem. 151 (2010) 121.

[65] O. Kassem, M. Saadaoui, M. Rieu, J.-P. Viricelle, A novel approach to a fully inkjet printed SnO 2-based gas sensor on a flexible foil, J. Mater. Chem. C 7 (2019) 12343.

[66] D.H. Kim, Y.S. Kim, J. Wu, Z. Liu, J. Song, H.S. Kim, Y.Y. Huang, K.C. Hwang, J.A. Rogers, Ultrathin silicon circuits with strain-isolation layers and mesh layouts for high-performance electronics on fabric, vinyl, leather, and paper, Adv. Mater. 21 (2009) 3703.

[67] H. Cheng, J. Wu, M. Li, D.-H. Kim, Y.-S. Kim, Y. Huang, Z. Kang, K. Hwang, J.A. Rogers, An analytical model of strain isolation for stretchable and flexible electronics, Appl. Phys. Lett. 98 (2011): 061902.

[68] A. Romeo, Q. Liu, Z. Suo, S.P. Lacour, Elastomeric substrates with embedded stiff platforms for stretchable electronics, Appl. Phys. Lett. 102 (2013) 131904.

[69] Y. Liu, Z. Liu, B. Zhu, J. Yu, K. He, W.R. Leow, M. Wang, B.K. Chandran, D. Qi, H. Wang, Stretchable motion memory devices based on mechanical hybrid materials, Adv. Mater. 29 (2017) 1701780.

[70] Y. Zhang, S. Wang, X. Li, J.A. Fan, S. Xu, Y.M. Song, K.J. Choi, W.H. Yeo, W. Lee, S.N. Nazaar, Experimental and theoretical studies of serpentine microstructures bonded to prestrained elastomers for stretchable electronics, Adv. Funct. Mater. 24 (2014) 2028.

[71] S. Xu, Y. Zhang, J. Cho, J. Lee, X. Huang, L. Jia, J.A. Fan, Y. Su, J. Su, H. Zhang, Stretchable batteries with self-similar serpentine interconnects and integrated wireless recharging systems, Nat. Commun. 4 (2013) 1543.

[72] Z. Wang, L. Zhang, S. Duan, H. Jiang, J. Shen, C. Li, Kirigami-patterned highly stretchable conductors from flexible carbon nanotube-embedded polymer films, J. Mater. Chem. C 5 (2017) 8714.

[73] A.D. Wilson, Review of electronic-nose technologies and algorithms to detect hazardous chemicals in the environment, Proc. Technol. 1 (2012) *453–463*. **1**, 453.

[74] C. Wongchoosuk, M. Lutz, T. Kerdcharoen, Detection and classification of human body odor using an electronic nose, Sensors 9 (2009) 7234.

[75] R. Maiti, L.-C. Gerhardt, Z.S. Lee, R.A. Byers, D. Woods, J.A. Sanz-Herrera, S.E. Franklin, R. Lewis, S.J. Matcher, M.J. Carré, In vivo measurement of skin surface strain and sub-surface layer deformation induced by natural tissue stretching, J. Mech. Behav. Biomed. Mater. 62 (2016) 556.

[76] B. Chen, K. Genovese, B. Pan, In vivo panoramic human skin shape and deformation measurement using mirror-assisted multi-view digital image correlation, J. Mech. Behav. Biomed. Mater. (2020) 103936.

[77] V. Wienert, H. Sick, Local thermal stress tolerance of human skin, Anasthesie, Intensivther. Notfallmed. 18 (1983) 88.

[78] H. Tian, H. Fan, M. Li, L. Ma, Zeolitic imidazolate framework coated ZnO nanorods as molecular sieving to improve selectivity of formaldehyde gas sensor, ACS Sens. 1 (2016) 243.

[79] R. Ye, D.K. James, J.M. Tour, Laser-induced graphene: from discovery to translation, Adv. Mater. 31 (2019) 1803621.

[80] R. Ye, D.K. James, J.M. Tour, Laser-induced graphene, Acc. Chem. Res. 51 (2018) 1609.

[81] M.G. Stanford, K. Yang, Y. Chyan, C. Kittrell, J.M. Tour, Laser-induced graphene for flexible and embeddable gas sensors, ACS Nano 13 (2019) 3474.

[82] J. Lin, Z. Peng, Y. Liu, F. Ruiz-Zepeda, R. Ye, E.L. Samuel, M.J. Yacaman, B.I. Yakobson, J.M. Tour, Laser-induced porous graphene films from commercial polymers, Nat. Commun. 5 (2014) 1.

[83] A. Das, B. Chakraborty, A. Sood, Raman spectroscopy of graphene on different substrates and influence of defects, Bull. Mater. Sci. 31 (2008) 579.

[84] L. Yang, N. Yi, J. Zhu, Z. Cheng, X. Yin, X. Zhang, H. Zhu, H. Cheng, Novel gas sensing platform based on a stretchable laser-induced graphene pattern with self-heating capabilities, J. Mater. Chem. 8 (2020) 6487.

[85] A. Lamberti, F. Clerici, M. Fontana, L. Scaltrito, A highly stretchable supercapacitor using laser-induced graphene electrodes onto elastomeric substrate, Adv. Energy Mater. 6 (2016) 1600050.

[86] Y. Du, J. Wang, Y. Zou, W. Yao, J. Hou, L. Xia, A. Peng, A. Alsaedi, T. Hayat, X. Wang, Synthesis of molybdenum disulfide/reduced graphene oxide composites for effective removal of Pb (II) from aqueous solutions, Sci. Bull. 62 (2017) 913.